# Influence of temperature on atomic layer epitaxial growth of indium nitride assessed with *in situ* grazing incidence small-angle X-ray scattering

Running title: Influence of temperature on atomic layer epitaxial growth of indium nitride assessed with *in situ* grazing incidence small-angle X-ray scattering

Running Authors: Woodward et al.

#### J.M. Woodwarda)

American Society for Engineering Education, 1818 N Street NW #600, Washington, DC 20036 (residing at U.S. Naval Research Laboratory)

## S.G. Rosenberg and A.C. Kozen

American Society for Engineering Education, 1818 N Street NW #600, Washington, DC 20036 (residing at U.S. Naval Research Laboratory)

#### N. Nepal and S.D. Johnson

U.S. Naval Research Laboratory, 4555 Overlook Avenue SW, Washington, DC 20375

## C. Wagenbach

Boston University, Division of Materials Science & Engineering, 590 Commonweath Avenue, Boston, MA 02215

#### A.H. Rowley and Z.R. Robinson

The College at Brockport - SUNY, Department of Physics, 350 New Campus Drive, Brockport, NY 14420

#### H. Joress

Cornell High Energy Synchrotron Source, Cornell University, Ithaca, NY 14853

#### K.F. Ludwig, Jr.

Boston University, Department of Physics and Division of Materials Science & Engineering, 590 Commonweath Avenue, Boston, MA 02215

#### C.R. Eddy, Jr.

U.S. Naval Research Laboratory, 4555 Overlook Avenue SW, Washington, DC 20375

The surface topological evolution during the growth of indium nitride (InN) by plasma-assisted atomic layer epitaxy (ALEp) on gallium nitride (GaN) (0001) substrates was studied using *in situ* real-time grazing incidence small angle X-ray scattering (GISAXS), for 180 °C, 250 °C, and 320 °C growth temperatures. The GISAXS data reveal that the ALEp growth of InN on GaN in this temperature range proceeds in a Stranski-Krastanov mode, in which the 2D-3D transition occurred after 2.3 monolayers for 180 °C, 1 monolayer for 250 °C and 1.5 monolayers for 320 °C. The corresponding initial island center-to-center distances were 7.4, 11.6, and 11.7 nm. Additionally, island coarsening was observed to increase with temperature. After 200 growth cycles, the mean island diameters were 3.9, 5.6, and 7.0 nm, and the mean island center-to-center distances were 8.6, 13.7, and 17.1 nm, for 180 °C, 250 °C, and 320 °C growth temperatures, respectively. For the 320 °C growth, the mean island shape was observed to gradually evolve from relatively mounded to cylindrical. These results are supported by atomic force microscopy and specular X-ray reflectivity.

# I. INTRODUCTION

Indium nitride (InN) is an attractive material for electronics and optoelectronics due to its excellent transport characteristics, 0.7 eV direct bandgap, unusually low conduction band minimum, wide phonon gap, radiation resistance, and intrinsic surface electron accumulation<sup>1</sup>. While InN is primarily recognized as a constituent of alloys with gallium nitride (GaN) for use in visible spectrum light emitting diodes<sup>2</sup>, these unique properties are promising for a wide range of device applications including high speed and high frequency

transistors<sup>3</sup>, chemical and biological sensors<sup>4,5</sup>, and topological insulator-based devices<sup>6,7</sup>. However, the growth of InN by conventional epitaxial methods, such as metalorganic chemical vapor deposition (MOCVD) and molecular beam epitaxy (MBE), is considerably more difficult than the growth of GaN and AlN, due to the low dissociation temperature and high vapor pressure of nitrogen over indium<sup>1</sup>.

Plasma-assisted atomic layer epitaxy (ALEp), a variant of plasma-assisted atomic layer deposition in which relatively higher temperatures are utilized to promote surface diffusion processes<sup>8</sup>, offers several potential advantages over conventional methods for the epitaxy for III-N materials and device structures. These advantages include significantly lower growth temperatures and highly controlled layer thicknesses, the latter of which is the result of the sequential pairs of self-limiting and self-terminating surface half-reactions that constitute the growth process. In recent years, significant progress in the growth of III-N films by ALEp<sup>9-12</sup> and low temperature ALD<sup>12-15</sup> has been achieved. However, ALEp is a relatively new method for III-N growth, and significant efforts will be required to better understand the nucleation and growth kinetics. To this end, grazing incidence small-angle X-ray scattering (GISAXS) has been previously utilized for the study of surface topological evolution during the ALEp growth of InN<sup>16,17</sup> and AlN<sup>18</sup> on a-plane Al<sub>2</sub>O<sub>3</sub> substrates. GISAXS is a non-destructive technique that can probe electron density fluctuations on length scales ranging from approximately 1 nm to 250 nm in an integral manner<sup>19</sup>, making it well-suited to the study of epitaxial growth. Furthermore, it is suitable to the 1-500 mTorr pressures in which ALEp growth is performed, in contrast to electron diffraction techniques such as reflection high energy electron diffraction which require high vacuum (HV).

In this work, we have investigated the epitaxial growth of InN on GaN (0001) substrates by plasma-assisted ALEp at three different temperatures using *in situ* real-time GISAXS, which was supported by *ex situ* atomic force microscopy (AFM) and specular X-ray reflectivity (XRR). Through a combination of direct analysis of the GISAXS patterns and Hankel transform-based numerical fitting, we observed that the ALEp growth of InN on GaN (0001) proceeds in a Stranski-Krastanov (SK) mode<sup>20</sup> in which 1-3 monolayers of 2D InN are grown before the onset of 3D island formation, and extracted the evolving sizes, shapes, and center-to-center distances of the island features. The temperature dependence of the InN critical thickness, island nucleation density, and coarsening behavior are discussed.

# II. EXPERIMENTAL

The GISAXS studies were enabled by the use of a custom ALEp reactor designed for *in situ* X-ray scattering experiments, featuring X-ray transparent beryllium windows of 250 µm thickness, both upstream and downstream of the sample platen, and the capability of mounting to an optical table with fine positioning control. The upstream window was attached to an extruded snout on the reactor, which decreased parasitic scattering. The reactor also used the same Veeco Fiji Gen 1 inductively coupled plasma source found on commercial systems. The temperature of the sample platen was measured by a Williamson Pro40 pyrometer. More detailed descriptions of the reactor have been published by Nepal et al<sup>16</sup>, Anderson et al<sup>18</sup>, and Rosenberg et al (in press).

# A. GaN substrate preparation and InN film growth

Bulk GaN substrates from Lumilog, previously diced into 1 cm<sup>2</sup> squares, were cleaned by swirling in sequential 5 minute baths of acetone, isopropanol, and deionized

water, then dried with N<sub>2</sub>. After the solvent clean, the substrates were subjected to a 10 minute UV-ozone clean in a Samco UV-1 followed by a 1 minute etch in 48% hydrofluoric acid, and a final rinse in deionized water. In prior work, Rosenberg et al determined by AFM and XPS that the application of this *ex situ* cleaning method to the Lumilog GaN substrates produces a smooth, stepped surface, with reduced carbon and oxygen impurities<sup>21</sup>. Upon completion of the *ex situ* cleaning process, the substrates were dried with N<sub>2</sub> and loaded into the reactor loadlock within 10 minutes in order to minimize reoxidation from the air. An additional *in situ* clean utilizing sequential series of atomic level processes (ALP) was performed in preparation for growth. All ALPs were performed while maintaining constant ultra high purity (UHP) Ar flows of 60 sccm through the metalorganic (MO) precursor manifold and 200 sccm through the plasma source, with an additional 75 sccm of UHP H<sub>2</sub> or UHP N<sub>2</sub> through the plasma source during the exposure of the substrate to plasma at 300 W forward power.

First, at 500 °C, the substrate was cleaned using 10 cycles of emulated gallium flash-off (GFO) ALP (consisting of trimethylgallium pulse, Ar purge, H<sub>2</sub> plasma exposure, Ar purge), 10 cycles of hydrogen clean ALP (H<sub>2</sub> plasma exposure, Ar purge), and 10 cycles of nitridation ALP (N<sub>2</sub> plasma exposure, Ar purge). The durations of the constituent subcycle processes are shown in Table I. The substrate was then cooled down to the intended InN growth temperature while maintaining the Ar flows, and then the 10 cycles of hydrogen clean and nitridation ALPs were repeated. The starting GaN (0001) surface was presumably terminated by nitrogen atoms due to the final nitridation ALP cycles immediately preceding growth. The number of cycles (10) and platen temperature (500 °C)

used for the GFO ALP were previously optimized by Rosenberg et al (in press) in other work.

TABLE I. The durations of the constituent sub-cycle processes for *in situ* clean ALPs and InN ALEp growth.

Process	MO pulse (msec)	Purge 1 (sec)	Plasma (sec)	Purge 2 (sec)
GFO ALP	60	10	30	20
Hydrogen clean ALP			30	10
Nitridation ALP			30	10
InN ALEp growth	60	10	20	28

InN films were grown on the prepared GaN substrates using temperatures of  $180\,^{\circ}\text{C}$ ,  $250\,^{\circ}\text{C}$ , and  $320\,^{\circ}\text{C}$ . All other growth parameters were identical. As with the ALPs, constant UHP Ar flows of  $200\,^{\circ}\text{C}$  secm through the plasma source and  $60\,^{\circ}\text{C}$  secm through the MO precursor manifold were maintained. The ambient pressure was  $2\times10^{-1}\,^{\circ}\text{torr}$ . The cation species was provided by  $60\,^{\circ}\text{millisecond}$  pulses of semiconductor grade trimethylindium (TMI), which was found in prior work to fully saturate the surface for self-limited growth  $^{10,16}$ . Each growth consisted of  $200\,^{\circ}\text{cycles}$  of  $60\,^{\circ}\text{second}$  duration per cycle. Each individual cycle consisted of  $4\,^{\circ}\text{sub-cycle}$  processes, the durations of which are tabulated in Table I. The sub-cycle processes are illustrated in Fig. 1, and are described in the following:

- 1. The surface is saturated by a pulse of TMI. Only a fraction of the available surface sites are accessible, due to the effects of steric hindrance<sup>22</sup>.
  - 2. Excess TMI and CH<sub>3</sub> byproducts produced by surface reactions are purged.

- 3. 75 sccm of N<sub>2</sub> is flowed through the plasma source and impinges the surface. After a 1 second delay, the plasma is activated at 300 W forward power (nominally 1-4 W reflected). The N<sub>2</sub> plasma reacts with the precursor-terminated surface to form InN. After 20 seconds of exposure, the plasma is deactivated, and 1 second later the N<sub>2</sub> flow is stopped.
  - 4. Residual nitrogen species and CH<sub>3</sub> produced by surface reactions are purged.

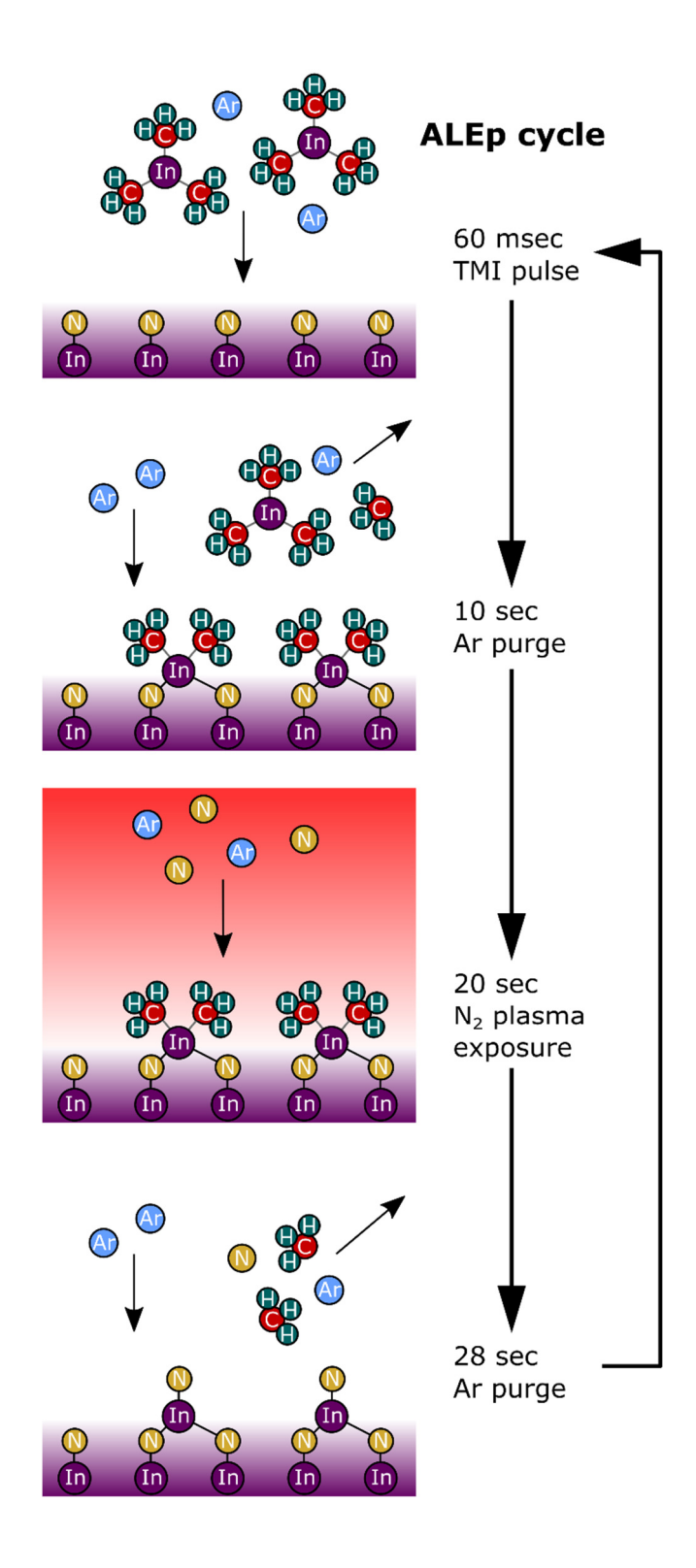


Fig. 1. The four sub-cycle process of the InN ALEp growth.

## B. GISAXS

GISAXS experiments were performed at the G3 beamline of Cornell High Energy Synchrotron Source (CHESS), using X-ray radiation with wavelength  $\lambda = 0.11048$  nm and incident beam angle  $\alpha_i = 0.8^{\circ}$ . This X-ray wavelength was not ideal, as its energy exceeds the Ga K-edge, and resulted in a weak but uniform background due to Ga fluorescence from the GaN substrates. Scattered X-rays were collected by a 2D Dectris 2M Pilatus detector using 1 second integration time for the first 8000 seconds (~ 133 cycles), and 6 second integration time for the remainder of the growth. The GISAXS geometry can be seen in Fig. 2(a), in which  $\mathbf{k_i}$  is the incident wavevector,  $\mathbf{k_f}$  is the exiting wavevector,  $\alpha_i$  is the incident angle,  $\alpha_f$  is the out-of-plane exit angle, and  $2\theta_f$  is the in-plane exit angle. These angles were converted to momentum transfer  $\mathbf{q}$  using

$$\begin{pmatrix} q_x \\ q_y \\ q_z \end{pmatrix} = \frac{2\pi}{\lambda} \begin{pmatrix} \cos(2\theta_f)\cos(\alpha_f) + \cos(\alpha_i) \\ \sin(2\theta_f)\cos(\alpha_i) \\ \sin(\alpha_f) + \sin(\alpha_i) \end{pmatrix}$$
 (1)

as such units are more physically meaningful and convenient for analysis.

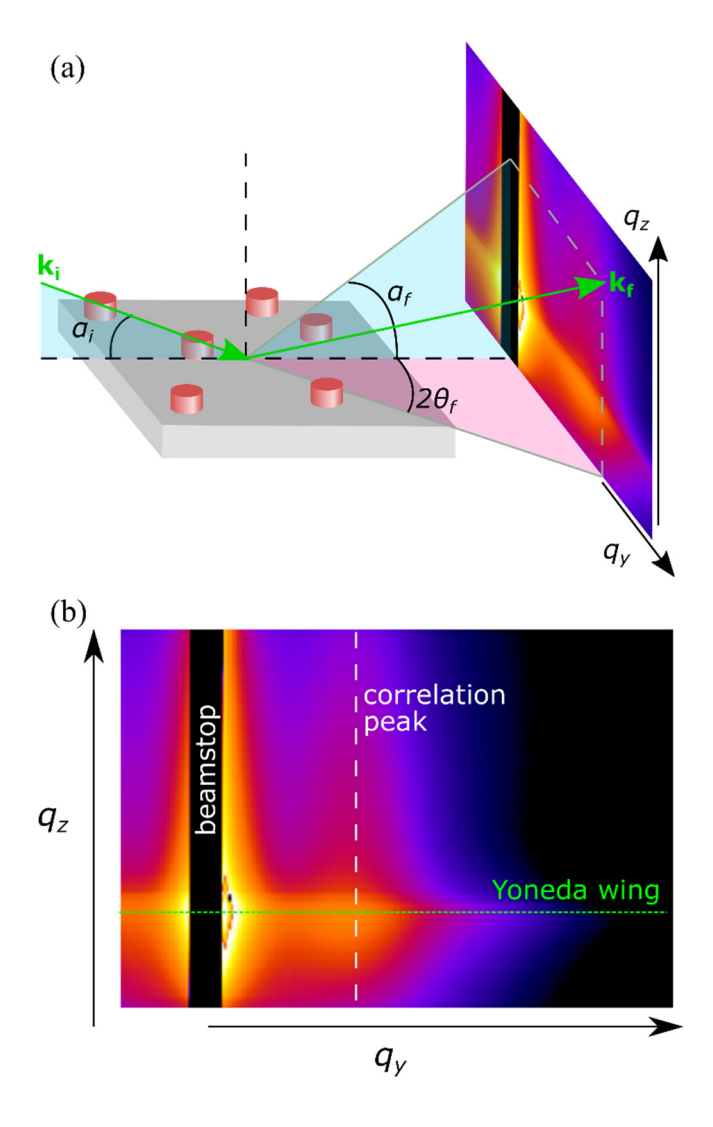


FIG. 2. (a) Illustration of the GISAXS geometry. Incident beam with wavevector  $\mathbf{k_i}$  impinges on the surface with out-of-plane angle  $\alpha_i$ , and scatters with wavevector  $\mathbf{k_f}$  with out-of-plane angle  $\alpha_f$  and in-plane angle  $2\theta_f$ . (b) Representative 2D GISAXS frame with annotated scattering features.

A representative 2D GISAXS frame from this work is shown in Fig. 2(b), with annotations to identify the most prominent features. A beam stop, which covered approximately  $|q_y| \leq .066 \text{ nm}^{-1}$ , was centered at  $q_y = 0$  so as to block the specular spot

and the near-specular (i.e.,  $q_y \approx 0$ ) diffuse scattering from saturating the detector. Intensity linecuts along the Yoneda Wing in the  $q_y$  direction, integrated vertically from approximately  $q_z = 1.00 \, \mathrm{nm}^{-1}$  to  $q_z = 1.08 \, \mathrm{nm}^{-1}$ , were extracted from the 2D detector frames using the Fiji<sup>23</sup> distribution of the ImageJ<sup>24</sup> image processing program and a custom plugin. The GISAXS profiles were not analyzed for  $q_y < 0$ , as they were symmetric about the  $q_z$  axis. The extracted data were analyzed using a series of custom tools implemented in the Python programming language with the Numpy<sup>25</sup>, Scipy<sup>26</sup>, and Matplotlib<sup>27</sup> libraries. The analysis techniques are described in detail in Section III.

## C. Ex situ characterization

Ex-situ specular XRR was performed at the G2 beamline at CHESS using X-ray radiation of wavelength 0.11048 nm and a Kappa-style six-circle diffractometer. The XRR data were analyzed in  $q_z' = \frac{4\pi}{\lambda} \sqrt{\cos\theta_c^2 - \cos\theta^2}$ , a refraction-corrected form of  $q_z$  (Ref.  $^{28}$ ), in which  $\theta_c$  is the critical angle. The thicknesses were then calculated as  $2\pi/\Delta q_z'$ , where  $\Delta q_z'$  is the spacing between adjacent Kiessig fringes. The fringe positions were determined by plotting  $q_z'^4 \times I(q_z')$  vs  $q_z'$ , in which the  $q_z'^4$  factor has compensated for the  $q_z'^{-4}$  dependence of the reflection coefficient square modulus<sup>28</sup>, and fitting the fringes independently as Gaussian functions. The island morphologies exhibited by the samples precluded standard fitting of the specular XRR data within the Parratt formalism, which assumes stratified media. Such data could potentially be modeled and fit within the DWBA, but that is beyond the scope of this work.

AFM topographs were acquired using a Park Systems XE-70 in tapping mode and probes with less than 10 nm tip radius of curvature. The topographical data was analyzed

in the scanning probe microscopy software, Gwyddion<sup>29</sup>. Island features were extracted from the height data background using the watershed algorithm, after which lateral and vertical size distributions were approximated by equivalent disc radius and maximum height values, respectively.

# **III. MODELLING AND ANALYSIS**

# A. Born Approximation and direct analysis

All X-ray scattering analysis in this work was performed within the Born Approximation (BA), which considers single scattering events involving a collection of scattering objects without interaction with the substrate<sup>19</sup>. We make the assumption that the islands are sufficiently monodisperse, which allows us to ignore an additional incoherent scattering term which would otherwise contribute to the intensity profile. The scattering intensity is then given by

$$I(q_{y}, q_{z}) = |F(q_{y}, q_{z})|^{2} S(q_{y}),$$
 (2)

in which form factor  $F(q_y, q_z)$  is the Fourier transform of the object shape and structure factor  $S(q_y)$  is the Fourier transform of the pair-correlation function of the object position. In this work, we considered the cylinder as a basic model for approximating island diameter. The corresponding form factor is represented by the analytical Fourier transform<sup>19</sup>

$$F_{cy}(q_y, R) = 2\pi R^2 \frac{J_1(q_y, R)}{q_y R},$$
 (3)

in which R is the radius of the cylinder and  $J_1$  is the Bessel function of first order, and we have dropped both an exponential and a cardinal sine factor with  $q_z$  dependencies

due to constraining our analysis to linecuts in the  $q_y$  direction. The method that we employed for evaluating island diameters using Eq. (3) is described in Section III.B.

As in our prior work<sup>17</sup>, we extracted various geometrical characteristics corresponding to collections of scattering objects, using direct analysis of specific features in the GISAXS patterns. The average island center-to-center distance – hereafter called "island spacing" – was approximated as  $2\pi/q_m$  where  $q_y = q_m$  is the position of the correlation peak (see Fig. 2(b)). Island shape was evaluated by Porod analysis in the high  $q_y$  limit, where the intensity decays as  $I(q_y) \propto q_y^{-n}$ . In the Porod analysis, the power-law exponent n is interpreted to depend on mean island shape<sup>30</sup>. For cylinders, n = 3, whereas for mounded shapes, e.g., hemispheres, n = 4. On a log-log scale, the power-law exponent n can be determined by linear fit of  $\log_{10}(I)$  vs  $\log_{10}(q_y)$ .

# B. Real space scattering model and Hankel analysis

Mean island diameters were determined using a real space scattering model in a similar manner to Refs. <sup>31–33</sup>. For a collection of identical scattering objects of in-plane circularly symmetric shape, the GISAXS scattering intensity can be described in real space, parallel to the plane of the substrate, as

$$I^{\mathrm{HT}}(r) \approx \Phi(r) + \Theta[P(r)-1],$$
 (4)

in which  $\Phi(r) = \Omega(r) \otimes \Omega(-r)^*$ ,  $\Omega$  is the island shape function,  $\Theta$  is the coverage of the surface by the islands,  $\otimes$  is the 2D in-plane convolution operator,  $I^{\rm HT}(r)$  denotes the in-plane Hankel transform of the GISAXS linecut  $I(q_y, q_z)$ , and P(r) is the in-plane pair correlation function. For small r the first term dominates, leading to

$$I^{\rm HT}(r) \propto \Phi(r) \pmod{r}$$
. (5)

Numerical fitting of Eq. (5) was performed by calculating  $I(q_y, q_z)$  from Eq. (2) with  $S(q_y) = 1$  (i.e., such that the intensity profile corresponds to island shape but not arrangement) using the cylinder shape function defined in Eq. (3), and then calculating the Hankel transform using the Quasi-discrete Hankel transform (QDHT) algorithm<sup>34</sup>.

## IV. RESULTS AND DISCUSSION

#### A. Nucleation

Fig. 3 shows the evolution of the Hankel transformed GISAXS data during the first 40 cycles of each growth process, in which the intensity distribution  $I^{HT}(r)$  for each cycle has been independently normalized for enhanced visibility. For all three growth temperatures, the Hankel transformed data for the first 11-25 cycles exhibited single peaks centered at r = 0 with broad tails, and the unnormalized magnitudes of the intensity distributions increased with each successive cycle. This lineshape is consistent with a 2D surface, and the increase in intensity could be explained by the greater atomic scattering factor of indium compared to that of gallium. Thus there was no nucleation delay, and the InN film growth initially proceeded in a 2D mode. A transition from 2D to 3D morphology was observed by the sudden narrowing of the peak centered at r = 0, concurrent with the appearance of a denuded zone (the blue region) followed by a correlation peak (the red region at higher r). The color maps for the contour plots are divergent, with red corresponding to positive values, white to zero, and blue to negative. Physically, the denuded zone represents a zone around each island within which adjacent islands are less likely to exist than in a completely uncorrelated system<sup>31</sup>. While the number of elapsed growth cycles prior to island formation varied significantly with temperature, no simple monotonic trend was found that accounts for all three samples. For InN grown at 180 °C, 250 °C, and 320 °C, island formation occurred during cycle 25, 11, and 16, respectively, and the initial mean island spacing was 7.4, 11.6, and 11.7 nm. These initial island spacings were calculated after the correlation peaks were sufficiently resolved (~20 cycles), rather than from the actual earliest appearances of the peaks. The initial spacings suggest that the initial areal density decreases as temperature increases, but saturates when a certain temperature threshold has been exceeded.

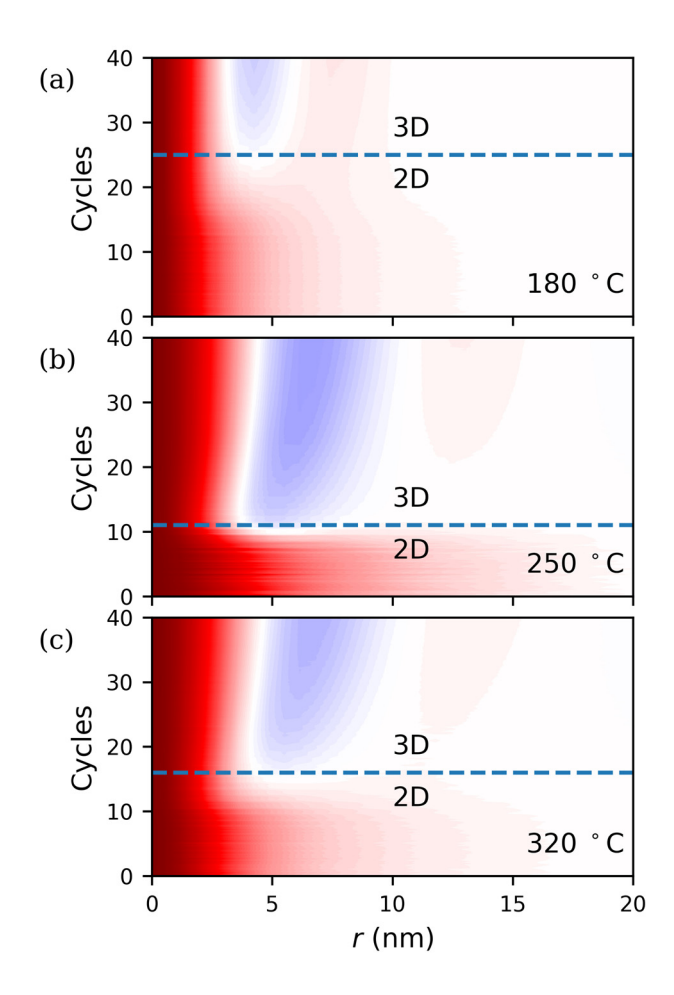


FIG. 3. Contour plots of the Hankel transformed GISAXS linecuts with increasing number of growth cycles, for growth temperatures of (a) 180 °C, (b) 250 °C, (c) 320 °C. Red represents positive values, white represents zero values, and blue represents negative values. The intensity distribution for each cycle has been independently normalized for visibility. The dashed blue line indicates the transition from 2D to 3D morphology.

The refraction-corrected specular XRR profiles, shown in Fig. 4(a), were multiplied by  ${q_z'}^4$  (Fig. 4(b)), and their Kiessig fringes were fit and analyzed as described in Section II.C. The InN films grown at temperatures of 180 °C, 250 °C, and 320 °C were found to be  $5.3 \pm .01$ ,  $5.0 \pm .01$ , and  $5.3 \pm .01$  nm thick, respectively. Equivalently, these

correspond to growth rates of 0.265 ± .0006, 0.251 ± .0006, and 0.266 ± .0003 Å/cycle. Thus the island formation at 180 °C, 250 °C, and 320 °C occurred after the growth of approximately 2.3, 1.0, and 1.5 monolayers of InN, respectively. A study of the epitaxial growth of InN on GaN using MBE by Dimakas et al<sup>35</sup> reported Stranski-Krastanov<sup>20</sup> growth mode with (1) a critical thickness of approximately 1 monolayer for temperatures below 350 °C, and (2) that the critical thickness increases with temperature. Our calculated InN film thicknesses at the onset of island formation for 250 °C and 320 °C are in agreement with both of these reported results. Our observation that island formation at the lowest growth temperature of 180 °C occurred at the greatest thickness of 2.3 monolayers could be explained by various mechanisms. One possible explanation is that the InN film has a lower degree of crystallinity, as this would presumably reduce the accumulation of strain and thus delay the 2D to 3D growth mode transition. Alternatively, the delay in island formation at 180 °C could be explained by insufficient adatom diffusion<sup>36</sup> or an activation barrier to the formation of 3D clusters<sup>37</sup>.

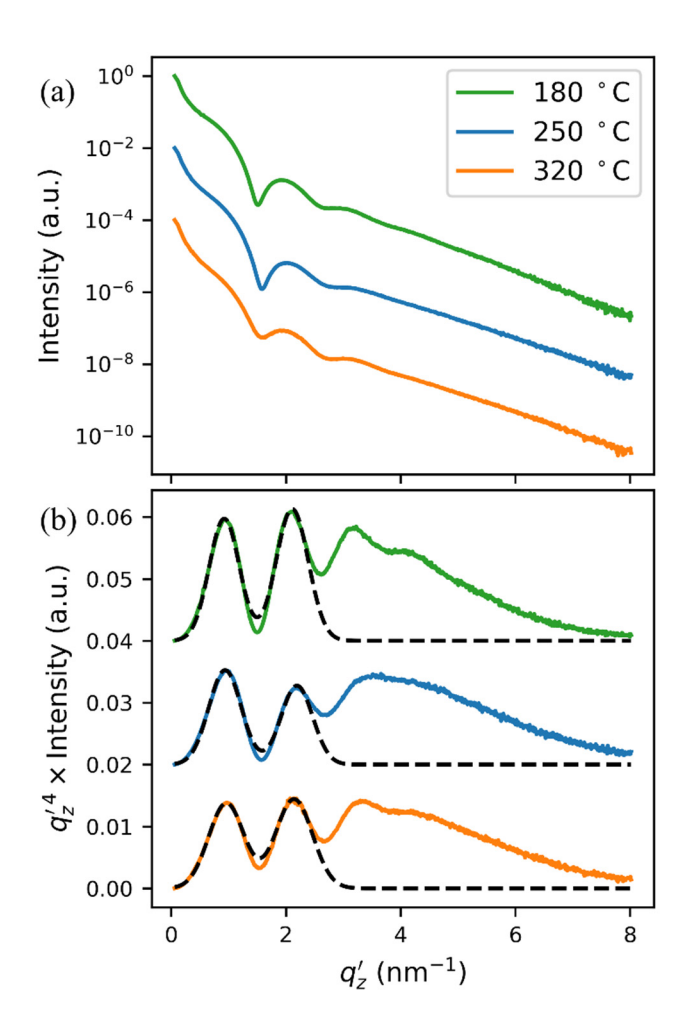


FIG. 4. Specular XRR profiles with refraction correction. (a) Intensity vs  $q'_z$ . (b)  ${q'_z}^4 \times$  Intensity vs  $q'_z$  with the first two Kiessig fringes fit independently as Gaussian functions.

# B. Growth kinetics

Fig. 5(a)-(c) shows contour plots of the GISAXS linecuts in which the colormaps correspond to log<sub>10</sub> of intensity. Contour plots of the Hankel transformed linecuts, with each transformed linecut individually normalized to 1 for visibility, are shown in Fig. 5(d)-(f) in which the color maps are divergent, with red representing positive values, white representing zero values, and blue representing negative values. As stated in Section IV. A., the Hankel transformed data indicate that the InN films initially grow in a 2D mode

without nucleation delay. The dotted horizontal lines indicate the cycle at which the onset of island formation occurred, and the black curves show the evolution of the mean island diameter, as determined by numerical fitting. The growth rates calculated in Section IV. A. are approximately equivalent to 0.1 monolayers of InN per cycle. The similar growth rates at all three temperatures indicate that the growth remains self-limited, even at the highest temperature of 320 °C. Sub-monolayer growth per cycle is an expected result, due to the effects of steric hindrance<sup>22</sup>.

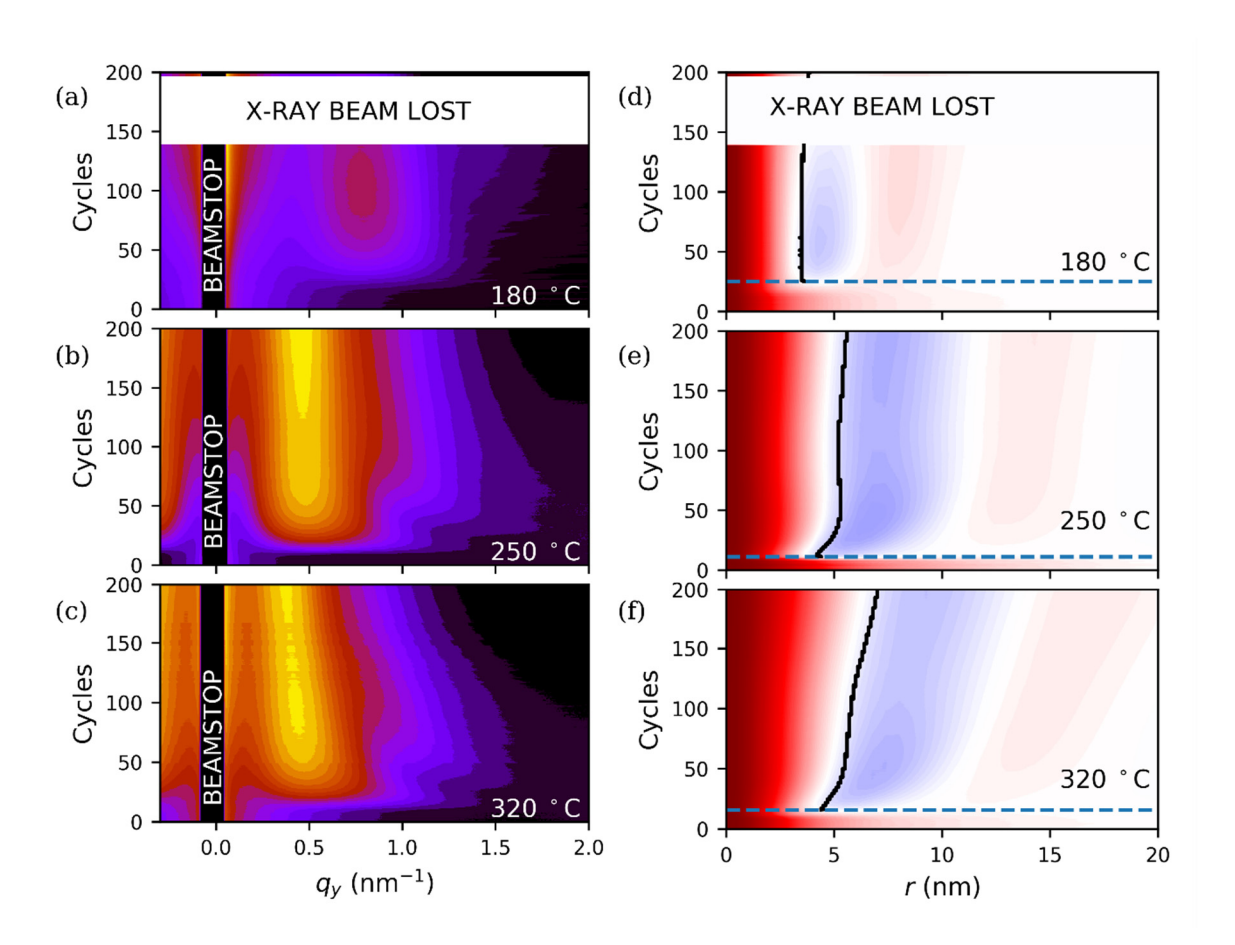


FIG. 5. Contour plots of the GISAXS linecuts along the Yoneda wing with increasing number of growth cycles for (a) 180 °C, (b) 250 °C, and (c) 320 °C. The colormap corresponds to log<sub>10</sub> of intensity. (d)-(f) Contour plots of the corresponding Hankel

transforms of the GISAXS linecuts, with black curves showing the mean island diameter. The color map is divergent, with red corresponding to positive values, white to zero values, and blue to negative values.

The mean island diameters and spacings are plotted in Fig. 6(a). Island coarsening is observed at the highest temperature of 320 °C, evidenced by steady increases in both mean island diameter and spacing. The mean island shape was also observed to gradually become more cylindrical, as seen in Fig. 6(b) by the decrease of the intensity decay power-law exponent *n* from 3.5 to 3.1 as the growth progressed. Coarsening behavior at lower temperatures was comparatively minimal, which suggests that the island coarsening at 320 °C is the result of increased adatom diffusion. For 250 °C, *n* remained nearly constant at 3.4. Porod analysis was not performed for the 180 °C growth, as the relatively poor signal to noise ratio was found to yield erroneously low values for *n*. No change to mean island diameter, spacing, or shape was observed to occur after completion of the growth process. The final values of the island geometric characteristics, as well as the InN thicknesses at which island formation was observed, are tabulated in Table II.

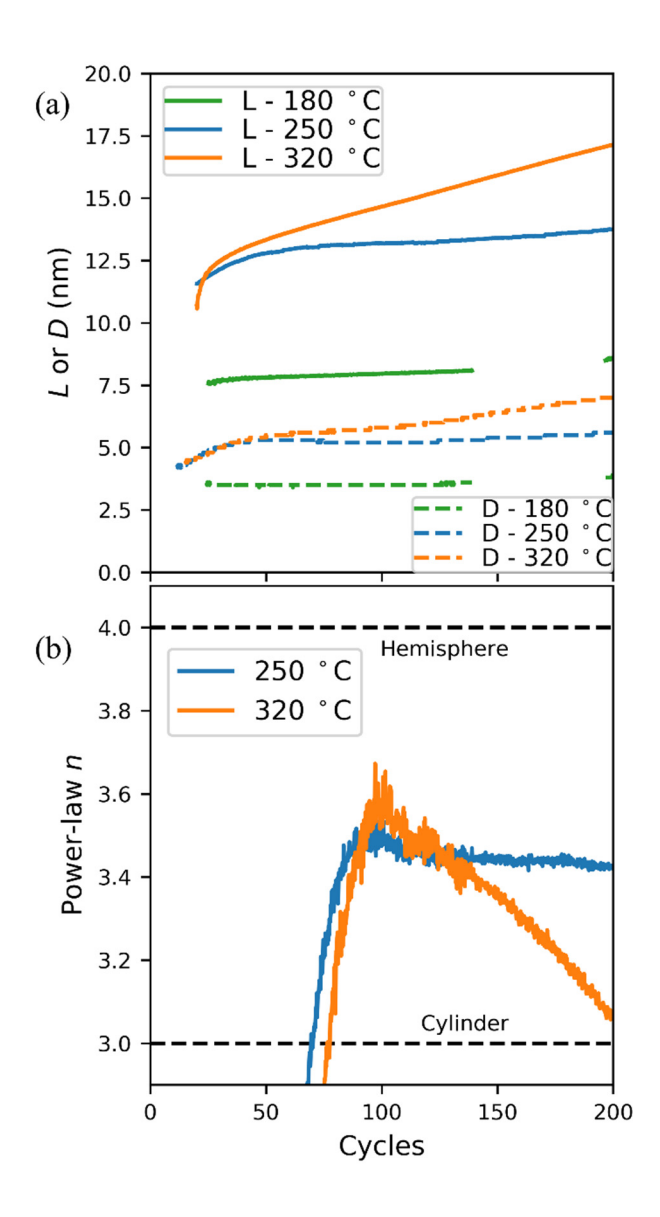


FIG. 6. (a). Evolution of mean island spacing L determined from correlation peak position and diameter D determined by numerical fitting of simulated scattering from cylinders. (b) Evolution of power-law exponent n from  $I(q_y) \propto q_y^{-n}$  fit of GISAXS linecuts at high  $q_y$ .

Table II. InN geometric characteristics determined by GISAXS.

Growth	2D-3D	Final	Final	Final
temperature	transition	diameter	spacing L	power-
(°C)	(monolayers)	D (nm)	(nm)	law n
180	2.3	3.9	8.6	

250	1.0	5.6	13.7	3.4
320	1.5	7.0	17.1	3.1

Fig. 7.(a)-(c) shows the AFM topographs corresponding to InN grown at 180 °C, 250 °C, and 320 °C, respectively, in which both the mean island diameter and mean interisland spacing are observed to have increased with temperature. This observation is supported by the trends in the calculated radial autocorrelation functions, shown in Fig. 7(d) for 250 °C and 320 °C growth only, and the island diameter distributions shown in Fig. 7(f). The mean island diameters and spacings, as determined by AFM, were larger than their GISAXS counterparts. This is an expected result, due to the known issues of broadening and smearing of the topography from tip-surface convolution. Nothing definitive can be inferred from the island height distributions, shown in Fig. 7(e), as the differences are not significant and could be affected by contributions from the underlying GaN substrate morphology.

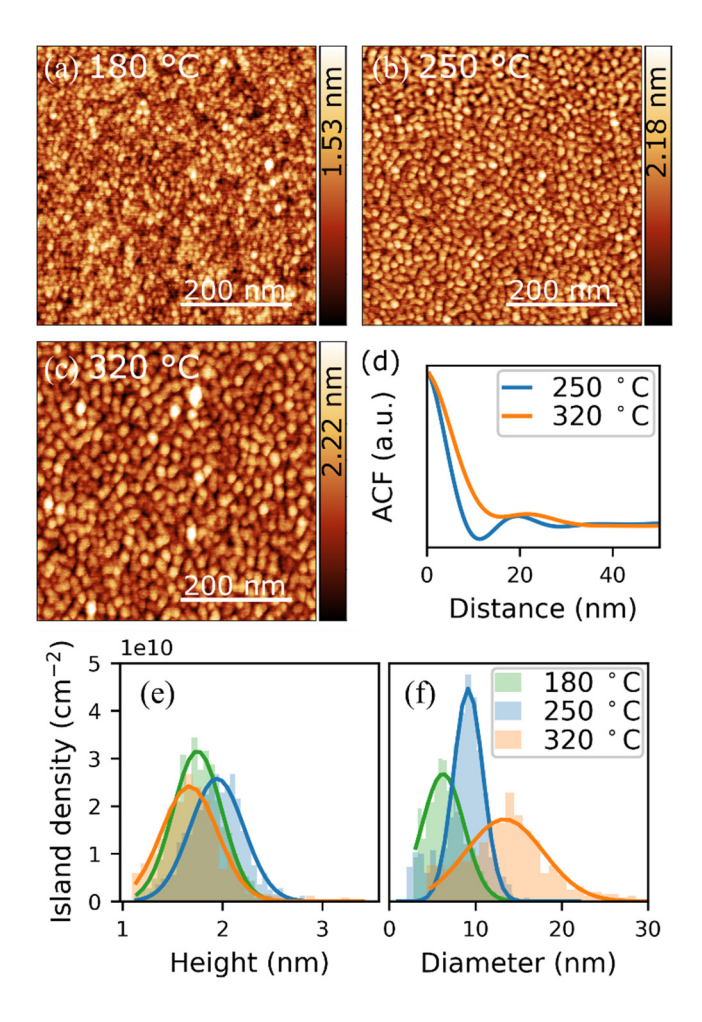


FIG. 7. (a)-(c) Ex situ  $500x500 \text{ nm}^2$  AFM topographs for InN grown at (a) 180 °C, (b) 250 °C, and (c) 320 °C. (d) Radial autocorrelation functions calculated from (b) and (c), in which the central peak at r=0 is observed to broaden and the secondary peak position is observed to shift to longer distance with increasing temperature, indicating an increase in island size and center-to-center distance, respectively. (e) Mean island height and (f) mean island diameter distributions.

# V. SUMMARY AND CONCLUSIONS

In summary, *in-situ* real-time grazing incidence small-angle X-ray scattering (GISAXS) was used to investigate the influence of temperature on the nucleation and

growth kinetics of the plasma-assisted atomic layer epitaxy (ALEp) of InN thin films on GaN (0001) substrates. The Hankel transforms of the GISAXS patterns show that the plasma-assisted ALEp growth of InN on GaN proceeds by Stranski-Krastanov growth mode. The InN monolayer coverage at which the 2D-3D transition occurred was observed to vary with growth temperature, though no simple monotonic trend could be established. For 180 °C, 250 °C, and 320 °C growth temperatures, the transition occurred after 2.3, 1.0, and 1.5 monolayers, respectively. These results for the 250 °C, and 320 °C growth are consistent with reported studies of InN on GaN by plasma-assisted molecular beam epitaxy<sup>35</sup>, whereas the delayed 2D-3D transition in the 180 °C growth could possibly be explained by a decreased crystallinity in the InN, an activation barrier to cluster formation, or insufficient adatom diffusion. Mean island center-to-center distances were determined from the positions of the GISAXS correlation peaks, and the island diameters were approximated by numerical fitting of the Hankel transformed GISAXS data using simulated scattering from cylinders. Mean island size and center-to-center spacing were observed to increase with temperature, and significant coarsening was observed at the highest temperature of 320 °C, which may be due to increased adatom diffusion. The Xray scattering data were consistent with mean island shapes that were not perfect cylinders or hemispheres, but could be consistent with e.g., truncated cones. For growth at 320 °C, the mean island shape gradually evolved towards cylindrical with increasing number of growth cycles.

The use of *in situ* real-time GISAXS has improved our understanding of the nucleation and growth kinetics for the ALEp growth of InN on GaN. While this work

focused on the influence of growth temperature, GISAXS will continue to be a vital tool as we investigate other growth parameters, such as the plasma chemistry, in future work.

# **ACKNOWLEDGMENTS**

Work at the U.S. Naval Research Laboratory is supported by the Office of Naval Research. The authors would like to acknowledge the assistance of Dr. Arthur Woll at the Cornell High Energy Synchrotron Source (CHESS), and Austin Hickman at Cornell University. Experiments at CHESS were supported by the National Science Foundation and the National Institutes of Health/National Institute of General Medical Sciences under NSF award DMR-1332208. ASEE-NRL PDF program. J.M. Woodward, S.G. Rosenberg, and A. C. Kozen would like to acknowledge the support of the American Society for Engineering Education and U.S. Naval Research Laboratory postdoctoral fellowship program. S.G. Rosenberg would also like to thank the Laboratory University Collaboration Initiative (LUCI) program, which was sponsored by the Basic Research Office, Office of Undersecretary of Defense for Research & Engineering for funding. The Boston University component of this work was supported by the National Science Foundation (NSF) under Grant No. DMR-1709380. The group from The College at Brockport would like to thank the Mancuso Summer research award for supporting this work.

1

<sup>&</sup>lt;sup>1</sup> J. Wu, J. Appl. Phys. **106**, 011101 (2009).

<sup>&</sup>lt;sup>2</sup> M.R. Krames, O.B. Shchekin, R. Mueller-Mach, G.O. Mueller, L. Zhou, G. Harbers, and M.G. Craford, J. Disp. Technol. **3**, 160 (2007).

<sup>&</sup>lt;sup>3</sup> M. Miao and C.G.V. de Walle, Appl. Phys. Express 8, 024302 (2015).

<sup>&</sup>lt;sup>4</sup> H. Lu, W.J. Schaff, and L.F. Eastman, J. Appl. Phys. **96**, 3577 (2004).

<sup>&</sup>lt;sup>5</sup> V. Jovic, S. Moser, S. Ulstrup, D. Goodacre, E. Dimakis, R. Koch, G. Katsoukis, L. Moreschini, S.-K. Mo, C. Jozwiak, A. Bostwick, E. Rotenberg, T.D. Moustakas, and K.E. Smith, Nano Lett. **17**, 7339 (2017).

- <sup>6</sup> M.S. Miao, Q. Yan, C.G. Van de Walle, W.K. Lou, L.L. Li, and K. Chang, Phys. Rev. Lett. **109**, 186803 (2012).
- <sup>7</sup> W. Pan, E. Dimakis, G.T. Wang, T.D. Moustakas, and D.C. Tsui, Appl. Phys. Lett. **105**, 213503 (2014).
- <sup>8</sup> C.R. Eddy, N. Nepal, J.K. Hite, and M.A. Mastro, Journal of Vacuum Science & Technology A: Vacuum, Surfaces, and Films **31**, 058501 (2013).
- <sup>9</sup> N. Nepal, S.B. Qadri, J.K. Hite, N.A. Mahadik, M.A. Mastro, and C.R. Eddy Jr, Appl. Phys. Lett. **103**, 082110 (2013).
- <sup>10</sup> N. Nepal, N.A. Mahadik, L.O. Nyakiti, S.B. Qadri, M.J. Mehl, J.K. Hite, and C.R. Eddy, Cryst. Growth Des. **13**, 1485 (2013).
- <sup>11</sup> N. Nepal, V.R. Anderson, J.K. Hite, and C.R. Eddy, Thin Solid Films **589**, 47 (2015).
- <sup>12</sup> P. Motamedi and K. Cadien, RSC Advances **5**, 57865 (2015).
- <sup>13</sup> C. Ozgit-Akgun, E. Goldenberg, A.K. Okyay, and N. Biyikli, J. Mater. Chem. C **2**, 2123 (2014).
- <sup>14</sup> A. Haider, S. Kizir, C. Ozgit-Akgun, E. Goldenberg, S.A. Leghari, A.K. Okyay, and N. Biyikli, J. Mater. Chem. C **3**, 9620 (2015).
- <sup>15</sup> H.-Y. Shih, W.-H. Lee, W.-C. Kao, Y.-C. Chuang, R.-M. Lin, H.-C. Lin, M. Shiojiri, and M.-J. Chen, Sci. Rep. **7**, 39717 (2017).
- <sup>16</sup> N. Nepal, J. Vac. Sci. Technol. A **35**, 031504 (2017).
- <sup>17</sup> N. Nepal, V.R. Anderson, S.D. Johnson, B.P. Downey, D.J. Meyer, Z.R. Robinson, J.M. Woodward, K.F. Ludwig, and C.R. Eddy, Journal of Vacuum Science & Technology A **ALD2019**, 020910 (2019).
- <sup>18</sup> V.R. Anderson, N. Nepal, S.D. Johnson, Z.R. Robinson, A. Nath, A.C. Kozen, S.B. Qadri, A. DeMasi, J.K. Hite, K.F. Ludwig, and C.R. Eddy, Journal of Vacuum Science & Technology A: Vacuum, Surfaces, and Films **35**, 031508 (2017).
- <sup>19</sup> G. Renaud, R. Lazzari, and F. Leroy, Surf. Sci. Rep. **64**, 255 (2009).
- <sup>20</sup> I.N. Stranski and L. Krastanow, Monatshefte für Chemie **71**, 351 (1937).
- <sup>21</sup> S.G. Rosenberg, D.J. Pennachio, C. Wagenbach, S.D. Johnson, N. Nepal, A.C. Kozen, J.M. Woodward, Z. Robinson, H. Joress, K.F. Ludwig, C.J. Palmstrøm, and C.R. Eddy, Journal of Vacuum Science & Technology A **37**, 020908 (2019).
- <sup>22</sup> R.L. Puurunen, Chemical Vapor Deposition **9**, 249 (2003).
- <sup>23</sup> J. Schindelin, I. Arganda-Carreras, E. Frise, V. Kaynig, M. Longair, T. Pietzsch, S. Preibisch, C. Rueden, S. Saalfeld, B. Schmid, J.-Y. Tinevez, D.J. White, V. Hartenstein, K. Eliceiri, P. Tomancak, and A. Cardona, Nature Methods **9**, 676 (2012).
- <sup>24</sup> C.T. Rueden, J. Schindelin, M.C. Hiner, B.E. DeZonia, A.E. Walter, E.T. Arena, and K.W. Eliceiri, BMC Bioinf. **18**, 529 (2017).
- <sup>25</sup> T. Oliphant, A Guide to NumPy (Trelgol Publishing, 2006).
- <sup>26</sup> E. Jones, T. Oliphant, P. Peterson, and others, (2001).
- <sup>27</sup> J.D. Hunter, Computing in Science & Engineering **9**, 90 (2007).
- <sup>28</sup> O. Durand and N. Morizet, Appl. Surf. Sci. **253**, 133 (2006).
- <sup>29</sup> D. Nečas and P. Klapetek, Open Physics **10**, 181 (2011).
- <sup>30</sup> C. Revenant, F. Leroy, R. Lazzari, G. Renaud, and C.R. Henry, Phys. Rev. B **69**, 035411 (2004).
- <sup>31</sup> J. Stangl, V. Holý, P. Mikulík, G. Bauer, I. Kegel, T.H. Metzger, O.G. Schmidt, C. Lange, and K. Eberl, Appl. Phys. Lett. **74**, 3785 (1999).

- <sup>32</sup> C. Frank, R. Banerjee, M. Oettel, A. Gerlach, J. Novák, G. Santoro, and F. Schreiber, Phys. Rev. B 90, 205401 (2014).
- <sup>33</sup> J.M. Woodward, A.Y. Nikiforov, K.F. Ludwig, and T.D. Moustakas, J. Appl. Phys. **122**, 065305 (2017).
- <sup>34</sup> L. Yu, M. Huang, M. Chen, W. Chen, W. Huang, and Z. Zhu, Opt. Lett., OL **23**, 409 (1998).
- 35 E. Dimakis, E. Iliopoulos, K. Tsagaraki, T. Kehagias, P. Komninou, and A. Georgakilas, Journal of Applied Physics **97**, 113520 (2005).

  36 B.G. Orr, D. Kessler, C.W. Snyder, and L. Sander, EPL **19**, 33 (1992).

  37 J.D. Weeks and G.H. Gilmer, in *Advances in Chemical Physics* (John Wiley & Sons,
- Ltd, 2007), pp. 157–228.